

Dynamic condensation of linker histone C-terminal domain regulates chromatin structure

Antoni Luque¹, Rosana Colleparado-Guevara², Sergei Grigoryev³ and Tamar Schlick^{1,4,*}

¹Department of Chemistry, New York University, 100 Washington Square East, New York, NY 10003, USA,

²University of Cambridge, Department of Chemistry, Lensfield Road, Cambridge CB2 1EW, UK, ³Department of Biochemistry and Molecular Biology, Penn State University College of Medicine, Hershey, PA 17033, USA and

⁴Courant Institute of Mathematical Sciences, New York University, 251 Mercer Street, New York, NY 10012, USA

Received March 18, 2014; Revised May 13, 2014; Accepted May 15, 2014

ABSTRACT

The basic and intrinsically disordered C-terminal domain (CTD) of the linker histone (LH) is essential for chromatin compaction. However, its conformation upon nucleosome binding and its impact on chromatin organization remain unknown. Our mesoscale chromatin model with a flexible LH CTD captures a dynamic, salt-dependent condensation mechanism driven by charge neutralization between the LH and linker DNA. Namely, at low salt concentration, CTD condenses, but LH only interacts with the nucleosome and one linker DNA, resulting in a semi-open nucleosome configuration; at higher salt, LH interacts with the nucleosome and two linker DNAs, promoting stem formation and chromatin compaction. CTD charge reduction unfolds the domain and decondenses chromatin, a mechanism in consonance with reduced counterion screening *in vitro* and phosphorylated LH *in vivo*. Divalent ions counteract this decondensation effect by maintaining nucleosome stems and expelling the CTDs to the fiber exterior. Additionally, we explain that the CTD folding depends on the chromatin fiber size, and we show that the asymmetric structure of the LH globular head is responsible for the uneven interaction observed between the LH and the linker DNAs. All these mechanisms may impact epigenetic regulation and higher levels of chromatin folding.

INTRODUCTION

The genome in eukaryotes is encoded in long double-stranded deoxyribonucleic acid (DNA) molecules that are densely packed with proteins to form the chromatin fiber. Chromatin's hierarchical structures govern transcription, replication, and repair of the genome (1,2). At the first level of organization, the DNA makes about 1.75 turns around

the histone octamer (two copies each of the core histones H2A, H2B, H3, and H4) to form the nucleosome. Linker DNA connects consecutive nucleosomes to form the 'beads-on-a-string array', which compacts at physiological salt conditions with added linker histones H1/H5. Higher levels of organization have remained controversial over more than three decades of research (3,4), inviting many experimental and computational studies (5).

Linker histones (LHs) are essential in higher organisms (6), regulating the transcription of genes and chromatin architecture (7). Depletion of LHs induces an expansion of chromatin *in vivo* (8,9) and destabilizes chromatin fibers *in vitro* (10,11). The compaction effect of LHs is attributed to the emergence of nucleosome stem motifs (12,13), which favor zigzag folding in 30-nm fibers (11,14,15). Because these processes depend on the reorganization of the unfolded LH regions upon binding to chromatin, an understanding of this mechanism is crucial.

LHs consist of a globular head (GH), and N-terminal (NTD) and C-terminal (CTD) domains (6,16). The ~80 amino acid GH was determined by X-ray (17) and nuclear magnetic resonance (NMR) (18) for avian and yeast LHs to be in the 'winged helix' family of DNA-binding proteins, conserved among H1 and H5 histones (19). The GH is essential for the binding of the LH in the nucleosome and stabilizes 10–20 bp of linker DNA (20). The exact position of the GH in the nucleosome is uncertain, although most studies indicate that it binds the nucleosome at the dyad axis or nearby (i.e. 1–2 DNA turns away) (16,21–23). The 20–35 amino acid NTD is intrinsically disordered and does not appear to affect higher-order chromatin compaction (24). The ~100 amino acid CTD is lysine-rich and intrinsically disordered (25), accounting for most of the sequence heterogeneity among LHs (26). The CTD is crucial for the compaction of chromatin (24) and is responsible for the high-affinity binding of LH to chromatin *in vivo* (27). Recent FRET experiments have shown that DNA binding triggers the condensation of the CTD, with folding dependent on whether the LH binds to the nucleosome or to naked DNA (28). In

*To whom correspondence should be addressed. Tel: +1 212 9983596; Fax: +1 212 9954152; Email: schlick@nyu.edu

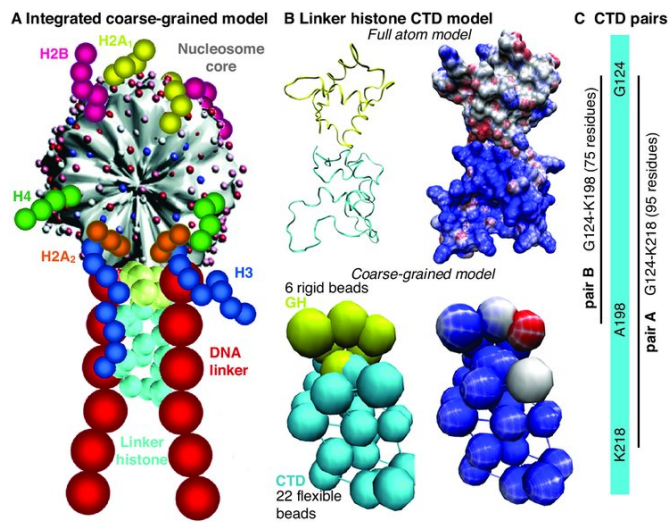


Figure 1. Integrated chromosome coarse-grained model with refined linker histone. (A) The nucleosome core includes the wrapped DNA and is modeled by 300 optimized surface pseudo-charges (smallest spheres colored in pink, magenta, and blue); linker DNA beads (large red spheres, six beads for 209bp NRL) are derived from the worm-like chain model; histone tails H2A1 (yellow), H2A2 (orange), H2B (magenta), H3 (blue), and H4 (green) have resolution of five amino acids per bead. The linker histone GH is represented by six rigid beads (gold) based on the full atomic structure of H1.4 (A and B), and the CTD is modeled as 22 flexible beads (cyan) of the same resolution of core histone tails (A and B). (B) Full-atom LH model shown as a ribbon representation and by Poisson-Boltzmann electrostatic surface (21,29) and our coarse-grained model with flexible CTD; the electrostatic representation has red-white-blue scale with range $[-10e, 10e]$. (C) Definition of amino acid pairs A and B for the rat H1.4 CTD, used in distance measurements in experiments (28).

addition, distances measured between CTD residues deviate from those predicted by CTD full-atom models (29). These clues suggest that CTD folding is dynamic and depends on both DNA binding and the chromatin environment.

Computational modeling has become essential for complementing experimental findings of biomolecular structures and associated processes (30,31). Modeling can help elucidate the atomic and molecular mechanisms behind the structural as well as regulatory roles of LHs in chromatin. Various chromatin models have characterized many key elements that control chromatin structure (reviewed in (5)). However, most computational and theoretical models, including our prior model, treat the effects of LH crudely or neglect them altogether. In turn, high-resolution LH models reveal neither the associated folding dynamics of the CTD nor the effect of LH in the global reorganization of chromatin upon LH binding (21,32).

Here, we enhance our mesoscale chromatin model with a refined GH and flexible CTD (see Figure 1). This refined LH model captures the spontaneous condensation of the CTD upon binding the nucleosome and reveals a dynamic charge neutralization mechanism between the CTD and linker DNAs. We also observe a synergistic role between the LH domains and nucleosome stem formation in chromatin fibers and explain the observed uneven organization of the linker DNAs by the intrinsic asymmetry of the GH. The CTD expansion that we discover for

smaller oligonucleosomes clarifies size variations observed experimentally. In addition, we show that unfolding of weakly charged CTDs decondenses chromatin, supporting the regulatory role of LH's post-translational modifications in transcription. These insights into the mechanism of CTD and chromatin condensation suggest specific ionic and amino-acid modifications that control chromatin organization and hence genomic accessibility and regulatory processes.

MATERIALS AND METHODS

Our coarse-grained model has characterized important structural mechanisms in chromatin, such as the role of electrostatics and core histone tails in fiber compaction (33), the dependence of chromatin architecture upon nucleosome repeat length (NRL) interfiber (15) and intrafiber variation (34), and the compaction and heteromorphism induced by LH and Mg^{2+} in equilibrated fibers (11) as well as fibers under tension (35,36). Our model also predicted that fibers with NRLs close to 177 and 187 bp adopt 30-nm zigzag structures (15,37), as recently revealed by high-resolution cryo-EM 3D reconstructions (38).

Our mesoscopic model has been developed for more than a decade, and our modeling strategies were recently detailed in references (15,33). In brief, the nucleosome core is approximated as a rigid surface made of 300 pseudo-charges, adjusted using Discrete Surface Charge Optimization (DiSCO) at different salt concentrations (39). The core histone tails are modeled as flexible charged beads with a resolution of five amino acids per bead using the Warshel–Levitt united-atom protein model (33). The linker DNA is modeled using an elastic worm-like chain of n_b spherical beads, where $n_b = 6$ for $NRL = 209$ bp. The negative charge of DNA is assigned at different salt concentrations using the Stigter's procedure (40), as detailed by Schlick *et al.* in reference (41). All elements interact with electrostatic and excluded volume terms as described in reference (15). The effects of monovalent ions are captured by adjusting the Debye–Hückel charges on all chromatin elements at different salt concentrations to reproduce atomistic properties of the electric field (33). The effect of divalent ions at low concentration is approximated by reducing the repulsion and persistence length of the linker DNAs (11). The model, however, cannot account for ionic effects between LH and nucleosomes at high monovalent salt concentrations (>200 mM) (42). Accordingly, our study focuses on physiological conditions below this ionic strength.

In our prior LH model, the linker histone H1.4 (rat) was approximated using three rigid charged-beads oriented through the nucleosome dyad axis (15). Here, we refine the LH model to capture the dynamics and flexibility of the C-terminal domain as well as the non-uniform charge distribution of the globular head (see Figure 1 and Supplementary Information for additional details). We derive the GH from the full atom structure of the rat H1.4 (21,29). A 6-bead model is obtained by combining the Shape-Based Coarse Grained (SBCG) method (43,44) with DiSCO (15,39) (see Supplementary Tables S.1 and S.2). We assume a symmetric positioning of the GH in accord with recent high resolution experiments (12) and orient GH in the dyad by the

full atom prediction model for GH and CTD of H1 (21,29) (see Figure 1 and Supplementary Figure S.1). We coarse-grain the highly basic and intrinsically unstructured CTD to capture the elasticity and electrostatics of the segment at different salt conditions using the same strategy applied for the core histone tails (see Supplementary Figure S.1A), with five amino acids per bead, so that 22 beads represent the 111-residue rat H1.4 CTD (109–219). The extended configuration of the CTD is 25 nm long. To fit the CTD in the medium linker DNA fibers, we use a compressed but elongated CTD starting configuration of length 10 nm consistent with FRET data (6) (see Supplementary Figure S.1B). The section *Refined LH model* in Supplementary Information contains an extended description of the new coarse-grained model, including the interactions and parameters of the LH.

We sample oligonucleosome conformations at constant temperature using five Monte Carlo (MC) moves to equilibrate and capture the multiscale dynamics of the system: (i) pivot, (ii) translation and (iii) rotation of DNA beads and nucleosome cores, (iv) regrowth of core histone tails, and (v) translation of LH CTD beads (see details in Supplementary Information).

We simulate oligonucleosomes of 3, 6, 12, and 24 residues with a uniform NRL of 209bp (six DNA linker beads) at temperature of 293 K. This NRL corresponds to differentiated cells, like chicken erythrocytes, where the fibers are fully loaded with LHs and the exchange rates are slow (45). Accordingly, we model fibers with one LH per nucleosome. Different salt concentrations of NaCl (5, 15, 80, and 150 mM) as well as low concentration of Mg^{2+} are examined for both our prior (11) and refined LH models. Different LH CTD charged states are considered for all salt conditions. Systems are equilibrated by 30 to 140 million MC steps for different starting configurations (Supplementary Figure S.2), which represent the classical zigzag and solenoid models for 30-nm chromatin fibers (5,15). We simulate at least eight trajectories per starting configuration. The simulations are long enough to guarantee the convergence of the energy as well as global and local quantities as demonstrated previously (15,37). The last 10 million steps are used for statistical analysis (with terminal nucleosomes omitted for LH properties), storing the fiber properties every 10 000 steps to guarantee the decorrelation of the averaged structures.

We characterize the structure of chromatin fibers with several standard properties described in the Supplementary Information and reference (15): sedimentation coefficient ($s_{20,w}$) (Eq. S.6), packing ratio (pr) (Eq. S.7), dimer (dd) and triplet (td) distances, entry-exit (α) (Supplementary Figure S.3) and triple (α) angles, and core-core interaction patterns ($I(k)$) (Eq. S.8). The LH CTD is characterized using the end-to-end distance (R_{ete}), radius of gyration (R_g), relative shape anisotropy (κ^2), and distance between amino acid pairs (see Supplementary Information for details).

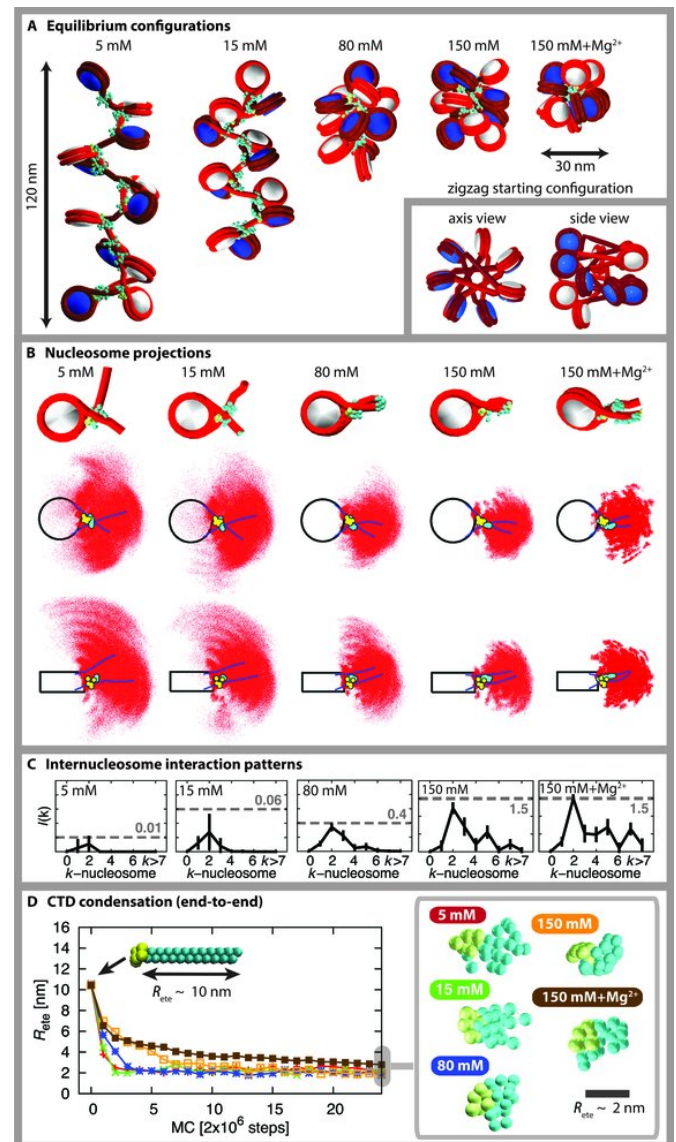


Figure 2. Equilibrium structures and chromosome conformations for 12×209 bp fibers at increasing salt milieus. (A) Equilibrium configuration and (B) nucleosome projections, including a characteristic chromosome snapshot as well as accumulated (red) and averaged (blue) projections of the linker DNA in the nucleosome top view and the dyad plane (side view), along with globular head position (yellow) and average CTD position (cyan). (C) Average core-core frequency interactions (with different scales) and (D) a condensation trajectory for CTD end-to-end distances, R_{ete} (see also Supplementary Figure S.14C).

RESULTS

LH CTD condensation: CTD neutralization mechanism

Our simulations from extended CTD conformations of 10 nm in agreement with FRET data (6) capture a dramatic condensation of the CTD within chromatin fibers. For each ionic state, Figure 2 shows representative fiber forms, top (nucleosome) and side (dyad) views of sampled linker DNA beads configurations (plus average linker DNA orientations), inter-nucleosome interaction patterns, and LH CTD end-to-end distances (R_{ete}) during fiber equilibration.

At low monovalent salt (5 and 15 mM), fibers adopt extended zigzag structures (Figure 2A). On average, the linker DNAs cross one another in the nucleosome plane as observed in Cryo-EM experiments (14,46) (Figure 2B). However, in the dyad plane, they remain uncrossed and form an open angle, which decreases with the salt concentration (Figure 2B). The CTD condensation is fast upon nucleosome binding (Figure 2D) and, overall, the chromosome adopts a bidente configuration where the LH interacts with the parent nucleosome core and the entry linker DNA (Figure 2B and Supplementary Figure S.4).

At higher monovalent salt (80 and 150 mM), chromatin becomes more compact (Figure 2A and B). This is consistent with the LH-dependent compaction observed *in vitro* on nucleosome arrays of similar size (10,11). In the compact fiber, an ordered zigzag pattern emerges with a sharp core–core peak interaction for second neighbor cores ($i \pm 2$) as well as a secondary peak associated to the interdigitation with fifth neighbors ($i \pm 5$) (Figure 2C). This compaction also reduces the linker DNA crossing angle in the nucleosome plane and the linker's range of fluctuations (Figure 2B). Compared to lower salt, the CTD condensation takes longer (more MC steps) (Figure 2D), but now the CTD bridges both linker DNAs, establishing a tridente interaction (nucleosome plus two linkers) and forming stems (Figure 2B and Supplementary Figure S.4).

As Figure 2D shows, the CTD reorganizes at all concentrations, from an extended, $R_{ete} \sim 10$ nm, to a condensed, $R_{ete} \sim 2-3$ nm, conformation. The equilibration length depends on the salt concentration, requiring 5, 5, 10, and 25 million MC steps to reach condensed conformations with $R_{ete} \sim 2$ nm at 5, 15, 80, and 150 mM NaCl, respectively. Figure 3B and C reveal a low average relative shape anisotropy, $\kappa^2 \sim 0.1$, and a low radius of gyration, $R_g \sim 3$ nm, indicative of a compact quasi-spherical shape. The independence of the CTD average conformation from the monovalent salt concentration suggests a charge neutralization condensation mechanism between the CTD and DNA, which we test next.

Indeed, CTD end-to-end distances for CTDs with neutral charge as well as one and two-thirds of the original charge in Figure 3A show a CTD decondensation upon charge reduction, forming an extended state for a neutral CTD ($R_{ete} \sim 10$ nm). The neutral and extended CTD adopt a radius of gyration almost twice the original one and a much more elongated shape, with $\kappa^2 \sim 0.5$ (Figure 3B and C). The fully and quasi-fully charged CTDs instead adopt similar structural properties, and the CTD with one-third of the charge leads to an intermediate state. In correspondence with our synergistic CTD/fiber condensation mechanism, Figures 2A and 3F show that the CTD charge reduction also decondenses and disrupts the chromatin fibers (see also Supplementary Figures S.5, S.6, S.7, and S.8). This unfolding resembles the behavior of fibers without LHs (see Supplementary Figure S.9).

Recent FRET experiments have investigated the condensation of the CTD in nucleosomes for H1 (H1.0 from *Xenopus laevis*) *in vitro* by measuring the distance between two pairs of residues of the CTD at 50 mM: 4.2 ± 0.2 nm for pair A (101–195) and 4.9 ± 0.3 nm for pair B (101–173) (28). H1.0 is shorter than H1.4 by 25 residues (196 versus

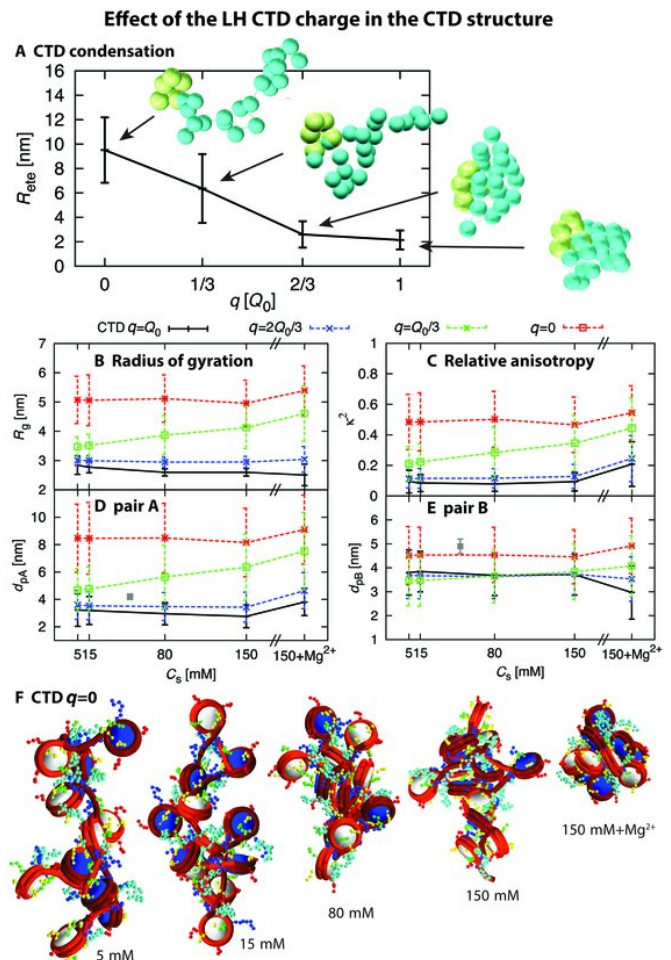


Figure 3. LH CTD structural properties for 12 x 209 bp fibers for different LH CTD charged states: neutral (dashed red), 1/3 charged (dashed green), 2/3 charged (dashed blue) and fully charged (solid black). (A) CTD condensation dependence on CTD charge illustrated by the average end-to-end radius, R_{ete} , overall LHs in a fiber. (B) Radius of gyration, Eq. S.11, (C) relative shape anisotropy, Eq. S.14, (D) pair A (124–218) amino acid distance and (E) pair B (124–198) amino acid distance. The error bars correspond to the standard deviation. In (D and E) we also plot the amino acid pair distances measured experimentally with FRET for H1(0) at 50 mM NaCl (28): pair $A_{exp} = 4.2 \pm 0.2$ nm (D) and pair $B_{exp} = 4.9 \pm 0.3$ nm (E). At the bottom of the figure we show equilibrium snapshots at different salt conditions for uncharged LH CTD (F).

219 amino acids). We associate pair A in our model with region 124–218 (95 residues starting from the penultimate amino acid) and pair B with region 124–198 (75 residues from the same starting point of pair A). Excellent agreement with experiments can be noted for Figure 3D and E, which plot equilibrium distances between corresponding pair beads, extrapolating values for 50 mM. Interestingly, our model and the experiments agree that, for fully charged CTDs, pair B is ~ 1 nm larger than pair A, despite being 22 residues shorter than pair A (see Figures 3D, B and 4B). H1.0 and H1.4 are both rich in lysines and have an identity of 46.4% for pair A (47). We also find that the CTD charge reduction increases distances for both pairs A and B, consistent with the unfolding of the CTD at these conditions.

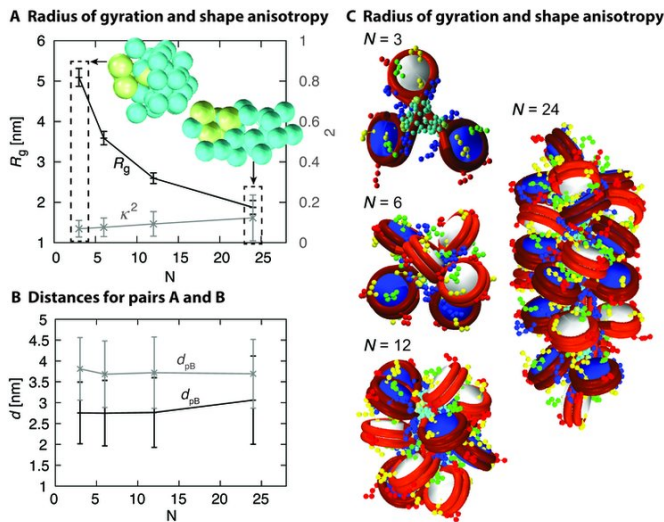


Figure 4. LH CTD structural properties for fibers with 3-, 6-, 12-, and 24-oligonucleosomes at 150 mM NaCl. (A) Radius of gyration, Eq. S.11, and relative shape anisotropy, Eq. S.14, as well as (B) distances between amino acid pairs A, G124-K218, and B, G124-A198 (as defined in Figure 1C). (C) Typical fiber configurations.

LH CTD configuration dependence on oligonucleosome size

Several studies have recently presented varying outcomes concerning the organization of nucleosome stems and LH CTD conformations using Cryo-EM, hydroxyl radical footprinting (12) and FRET (28) for mono-, di- and trinucleosomes.

To help interpret observations, we examine fiber properties for 3, 6, 12, and 24 nucleosomes at 150 mM NaCl in Figure 4, Supplementary Figures S.10 and S.11. For small fibers, we see that the average dimer distance is shorter and the triplet distance, triplet angle, as well as entry-exit angle are all larger, although the values stabilize for 12-oligonucleosomes. Figure 4A shows that the structural properties of the LH CTD exhibit a more complex behavior. While the shape anisotropy is small for all oligonucleosomes, average values and associated fluctuations increase with fiber size, indicating a richer combination of quasi-spherical and slightly elongated CTD conformations. The radii of gyration strongly increase for small oligonucleosomes and, for trimers, adopt a value of ~ 5 nm with a quasi-spherical CTD. Despite the divergence in R_g , Figure 4B shows that the distances between the pairs separated by 95 (pair A) and 75 (pair B) residues remain relatively constant, as found experimentally. More detailed insights into these structural changes in CTD folding demand both higher resolution FRET experiments and all-atom modeling.

That both local structural properties of chromatin fibers and the conformation of the LH CTD depend on the array size is consistent with our charge neutralization mechanism. Our quasi-spherical CTDs for small oligonucleosomes and more elongated configurations for larger fibers can be explained by greater exposure to solvent for small oligonucleosomes. At the same time, the physico-chemical properties of the CTD stabilize interactions between specific residues

independent of size. We also find that 12-oligonucleosome fibers are representative for evaluating structural properties.

Chromosome asymmetry and heteromorphicity

The LH globular head provides additional protection against enzymatic and chemical hydrolysis of both linker DNAs at the entry/exit region of the nucleosome (12,20). Earlier structural experiments suggested that this protection is symmetrical, about 10 bp per linker DNA (12), but recent biochemical experiments (48) using a refined nuclease technique account for DNA sequence bias and demonstrate that H1 confers an uneven protection of 11–12 and 8–10 bp to the entry and exit linker DNAs, respectively. Complementary high-resolution models and experiments, however, suggest that in this case the GH occupies a symmetric position in the nucleosome, contacting the dyad axis (12,20,22). Is there a source of asymmetry in the GH's protection of linker DNAs and, if so, what is its origin?

Our chromosome configurations for 12-unit oligonucleosomes at different salt concentrations in Figure 2B show that the average position of the linker DNAs is asymmetric with respect to the dyad axis near the GH for all conditions. In the nucleosome (top view) plane, the linker DNAs cross at a point that deviates from the dyad axis; in the dyad plane (side view), the linker DNAs do not cross and both tend to be oriented toward the top side of the nucleosome. Thus, the uneven protection provided by the LH is captured by our model. To determine the mechanism responsible for this asymmetry, at 150 mM NaCl we compare our refined model for both the GH and CTD to other LH models: our prior symmetrical LH model made of three rigid beads (one for GH and two for CTD) oriented through the dyad axis (Supplementary Figure S.1) and a hybrid model of one bead for GH with our refined CTD (22 beads). We see from the chromosome projections in Supplementary Figure S.12 that the two simpler LH models (with a one-bead GH) lead to nucleosomes where the linker DNAs adopt symmetrical configurations on average in both the nucleosome and dyad planes, in contrast to our refined GH model (see Figure 2B). These findings pinpoint the GH asymmetrical structure and charge distribution (see Figure 1B) as responsible for the asymmetric organization of the chromosome. Accordingly, the asymmetric GH is likely responsible for the uneven protection of the linker DNAs against enzymatic digestion.

The above biochemical studies are bulk experiments that provide an average picture of the chromosome, but do not reveal actual configurations of individual nucleosomes. Our average chromosome geometries are consistent with experimental data and offer additional insights into the structure of individual nucleosomes in a fiber. The red regions in Figure 2B show that chromosomes span wide range of configurations. In fact, even at 150 mM NaCl, when the zigzag pattern is prominent ($i \pm 2$ peaks in the internucleosome patterns), the accommodation of chromosomes in a fiber is non-uniform. Representative individual chromosomes in Supplementary Figure S.13 show qualitative deviations from average states. This non-uniform organization of chromosomes is a general feature of chromatin organization that emerges independently on the type of LH model

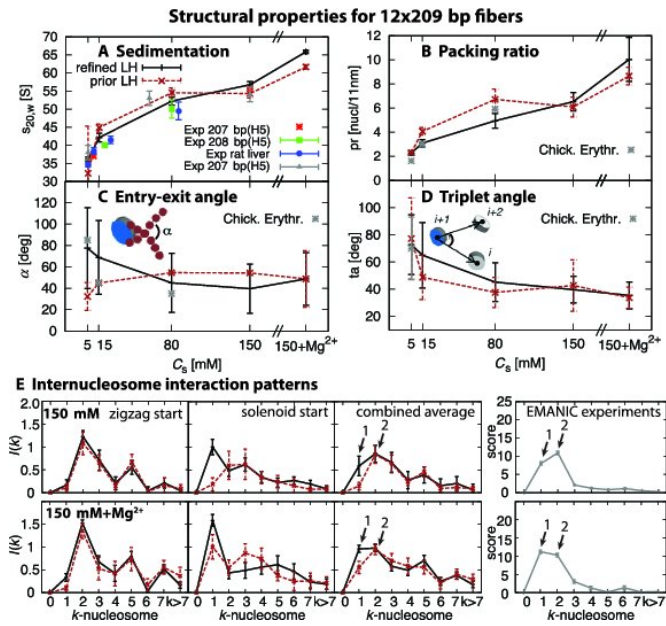


Figure 5. Structural properties for 12 x 209 bp as a function of salt for refined (solid black) and prior (dashed brown) LH. (A) Sedimentation coefficient, (B) packing ratio, (C) entry-exit angle (see definition in S.3), and (D) triplet angle. Error bars correspond to standard deviation. Experimental values for the sedimentation (A) are obtained from 12-oligonucleosomes made of 207 bp (11) (red) and 208 bp (49) (green), native chromatin from rat liver nuclei with an NRL \sim 200 bp (50) (blue), and 12 x 207 bp fibers (gray). Other experimental dots are associated with native chromatin fibers of chicken erythrocytes and are extracted from references (14) (B and C) and (46) (D). (E) Compare internucleosome interactions for 150 mM (top) and 150 mM with Mg^{2+} (bottom) from zigzag and solenoid starting configurations (six plots) and measured patterns from EMANIC (11).

used. Such an intrinsic heteromorphic mechanism (5,11) is likely enhanced by sequence specificity and regulatory factors.

Chromatin compaction dependence on salt concentration

Many experiments *in vitro* utilize fibers of 12 nucleosomes to elucidate the structural properties of chromatin (11,49,50). Accordingly, in Figure 5A we compare sedimentation coefficients obtained at different salt concentrations to those obtained with our mesoscale model. The NRLs for the experimental fibers range from 200 to 209 bp, similar to the NRL of 30-nm model fibers of chicken erythrocyte in differentiated cells (51). All fibers adopt similar sedimentation coefficients that increase with the salt concentration and are in good quantitative agreement with our 12 x 209 bp mesoscale chromatin model.

High-resolution structural techniques, like Cryo-EM, also characterize the packing ratio of chromatin fibers and show the increased density of nucleosomes (through the longitudinal axis of the fiber). Our comparison in Figure 5B shows excellent quantitative agreement. Figure 2A displays the corresponding equilibrium configurations of fibers at the different salt concentrations.

An experimental characterization of fiber local structural properties is challenging due to the high compaction adopted by chromatin at physiological conditions, but mea-

surements can be reconstructed from Cryo-EM data (14). Figure 5C compares measured experimentally entry-exit angles, which decrease upon salt concentration, with our results for 12x209bp models. Excellent agreement can be noted. The reduction of this angle corresponds to the formation of nucleosome stems. This stem is favored by the contact of the GH and CTD with both linker DNAs. (Note that our computed triplet angle is very similar to the entry-exit angle (see Figure 5D); this useful relationship is significant because the definition of the triplet angle is more precise than the definition of the entry-exit angle, see Supplementary Figure S.3). Figures 5C and D show that our computed values are also in good agreement with recent measurements of the triplet angle of chicken erythrocyte fibers at 5 mM of monovalent salt by Scheffer *et al.* (46) and entry-exit angle derived from Bednar *et al.* (14). Dimer distances measured at 5 mM monovalent salt are also in good agreement (see Supplementary Figure S.14A).

Figure 5 also displays structural properties for the prior LH model, which is generally in good agreement with experiments. However, the refined LH model reproduces better most structural experimental data, including the increase of $i \pm 1$ interactions when starting from solenoid configurations, in accordance with EMANIC experiments (11) (Figure 5E).

Effect of Mg^{2+}

Using our simplified treatment of moderate Mg^{2+} concentration (reduction of the DNA persistence length and enhanced interactions between linker DNAs) (11), Figure 5A and B show that divalent ions lead to higher sedimentation and packing ratio values, even for uncharged CTDs (see Figure 3F and Supplementary Figure S.7). The triplet angle and the pattern of the zigzag fiber are similar to the case of monovalent salt at 150 mM, although long-range interactions are stronger.

Importantly, divalent ions affect the organization of the CTD in several ways. For highly charged CTDs, the radius of gyration remains stable, but the anisotropy increases, leading to a more elongated conformation (see Figure 3C). This reconfigured CTD structure has an opposite effect to pairs A and B, so that distances become similar, $d_{pA} \simeq d_{pB}$. Our snapshots in Figure 3F and Supplementary Figure S.5 show that, at reduced CTD charges, the LH CTD escapes from the interior of the highly condensed fibers, because the charge neutralization mechanism cannot counteract the steric effects, and entropy favors these highly dynamic states. This important effect points to a potential regulatory mechanism in chromatin and shows that Mg^{2+} -induced linker DNA charge neutralization can mimic the stabilization role of the CTD on nucleosome stems.

DISCUSSION

Our enhanced chromatin mesoscopic model with flexible LHs reveals, for the first time, the synergistic condensation between LH CTD and the overall chromatin fiber organization. The CTD condensation in the nucleosome occurs dynamically with other nucleosome components and is controlled, in part, by a charge neutralization mechanism

with the linker DNAs driven by 30–50 positively charged CTD residues. This mechanism explains similar general behavior for different linker histone variants with similarly charged CTDs (H1c, H1e, H1⁰) (9). Highly charged CTDs condense and compact chromatin more tightly, therefore favoring genome silencing, consistent with structural data and regulation activity reported for the highly charged H5 in chicken erythrocyte (52,53). Analogously, lower-charged CTDs adopt variable positions that depart from the interior of compact fibers, enhancing genomic accessibility and generating potential long-distance interactions with other protein remodeling or nuclear elements.

A dynamic CTD works in tandem with the GH to stabilize nucleosome stems by bridging the two DNA linkers, leading to a tridentate interaction of the LH in the nucleosome (two DNA linkers plus the nucleosome core). Thus, it is not a stepwise process whereby CTD folds and then compacts chromatin structure but rather a dynamic interplay between CTD condensation and chromatin compaction. For small oligonucleosomes, for instance, the CTD expands, which could explain observed extended configurations of the CTD upon binding protein-free DNA (28). CTD conformations also depend on its charge, which might promote variations in folding observed for different LH types (6,29). Interestingly, despite our LH positioning in the dyad axis, the tridentate interaction with the nucleosome leads to an asymmetric chromatosome organization, where the entry linker DNA is closer to the LH than the exit linker DNA. This is due to the asymmetric structure of the GH and could explain recent experiments that measured a related uneven protection of the linker DNAs by LH (48). The fact that GH favors the interaction with one linker DNA is also consistent with *in vivo* mapping of the H1 interaction surface in the nucleosome (54) and NMR *in vitro* experiments of the chromatosome (23); the latter work also observes that one of the two H2A core histone tails is involved in the LH-nucleosome complex, in agreement with our model (see Supplementary Figure S.15). In addition, Supplementary Figure S.15 shows that, besides H2A2 tails, H3 tails exhibit a significant interaction with parent DNA linkers in the asymmetric tridentate configuration.

The net positive charge of the CTD varies among LH variants and can be decreased by post-translational modifications such as lysine acetylation (55), serine, threonine and tyrosine phosphorylation (56), and arginine citrullination (57). Our findings suggest that such charge reduction, along with acetylation of the lysine-rich core histone tails, should enhance more open structures and nucleosome accessibility, thus favoring transcription. This charge dependent mechanism could also explain experiments of LH phosphorylation, which mimic the effect of LH unbinding in chromatin decondensation (56); it also supports the condensation of chromatin observed in the dephosphorylation of H1 in differentiated cells (58). Additionally, the impact of the CTD net charge reduction is compatible with the decondensation of chromatin observed *in vitro* in the absence of LHs (3). The integrated view of the LH dynamic structure and chromatin architecture presented here establishes a framework for further interrogation of the structural role and regulatory mechanisms of LH variants as well as LH modifications in chromatin structure and function.

SUPPLEMENTARY DATA

Supplementary Data are available at NAR Online.

ACKNOWLEDGMENTS

We thank N.R. Chandra and M.R.S. Rao for providing the structure of the rat H1d linker histone, L. Fan and V.A. Roberts for facilitating their coordinates of H5 in the nucleosome, as well as G. Ozer for his insights concerning this work and J. Hayes for sharing unpublished data. Computing support from the NYU HPC USQ, BOWERY, and Cardiac clusters as well as Blue Gene at CCNI is also acknowledged.

Conflict of interest statement. None declared.

REFERENCES

- Felsenfeld, G. and Groudine, M. (2003) Controlling the double helix. *Nature*, **421**, 448–453.
- Szerlong, H. and Hansen, J. (2011) Nucleosome distribution and linker DNA: connecting nuclear function to dynamic chromatin structure. *Biochem. Cell Biol.*, **89**, 24–34.
- Grigoryev, S. and Woodcock, C. (2012) Chromatin organization – the 30 nm fiber. *Exp. Cell Res.*, **318**, 1448–1455.
- Quénet, D., McNally, J. and Dalai, Y. (2012) Through thick and thin: the conundrum of chromatin fibre folding *in vivo*. *EMBO Rep.*, **13**, 943–944.
- Schlick, T., Hayes, J. and Grigoryev, S. (2012) Towards convergence of experimental studies and theoretical modeling of the chromatin fiber. *J. Biol. Chem.*, **287**, 5183–5191.
- Caterino, T. and Hayes, J. (2011) Structure of the H1 C-terminal domain and function in chromatin condensation. *Biochem. Cell Biol.*, **89**, 35–44.
- Misteli, T., Gunjan, A., Hock, R., Bustin, M. and Brown, D. (2000) Dynamic binding of histone H1 to chromatin in living cells. *Nature*, **408**, 877–881.
- Fan, Y., Nikitina, T., Zhao, J., Fleury, T., Bhattacharyya, R., Bouhassira, E., Stein, A., Woodcock, C. and Skoultchi, A. (2005) Depletion of histone H1 in mammals alters global chromatin structure but causes specific changes in gene regulation. *Cell*, **123**, 1119–1212.
- Popova, E., Grigoryev, S., Fan, Y., Skoultchi, A., Zhang, S. and Barnstable, C. (2013) Developmentally regulated linker histone h1c promotes heterochromatin condensation and mediates structural integrity of rod photoreceptors in mouse retina. *J. Biol. Chem.*, **288**, 17895–17907.
- Routh, A., Sandin, S. and Rhodes, D. (2008) Nucleosome repeat length and linker histone stoichiometry determine chromatin fiber structure. *Proc. Natl. Acad. Sci. U.S.A.*, **105**, 8872–8877.
- Grigoryev, S., Arya, G., Correll, S., Woodcock, C. and Schlick, T. (2009) Evidence for heteromorphic chromatin fibers from analysis of nucleosome interactions. *Proc. Natl. Acad. Sci. U.S.A.*, **106**, 13317–13322.
- Meyer, S., Becker, N., Syed, S., Goutte-Gattat, D., Shukla, M., Hayes, J., Angelov, D., Bednar, J., Dimitrov, S. and Everaers, R. (2011) From crystal and NMR structures, footprints and cryo-electron-micrographs to large and soft structures: nanoscale modeling of the nucleosomal stem. *Nucleic Acids Res.*, **39**, 9139–9154.
- Bussiek, M., Tóth, K., Schwarz, N. and Langowski, J. (2006) Trinucleosome compaction studied by fluorescence energy transfer and scanning force microscopy. *Biochemistry*, **45**, 10838–10846.
- Bednar, J., Horowitz, R., Grigoryev, S., Carruthers, L., Hansen, J., Koster, A. and Woodcock, C. (1998) Nucleosomes, linker DNA, and linker histone form a unique structural motif that directs the higher-order folding and compaction of chromatin. *Proc. Natl. Acad. Sci. U.S.A.*, **95**, 14173–14178.
- Perišić, O., Collepardo-Guevara, R. and Schlick, T. (2010) Modeling studies of chromatin fiber structure as a function of DNA linker length. *J. Mol. Biol.*, **403**, 777–802.

16. Jerzmanowski, A. (2004) The linker histones. In: Zlatanova, J. and Leuba, S.H. (eds.), *Chromatin Structure and Dynamics: State-of-the-Art*, Elsevier B.V. 75–102.
17. Ramakrishnan, V., Finch, J., Graziano, V., Lee, P. and Sweet, R. (1993) Crystal structure of globular domain of histone H5 and its implications for nucleosome binding. *Nature*, **362**, 219–223.
18. Ali, T., Coles, P., Stevens, T., Stott, K. and Thomas, J. (2004) Two homologous domains of similar structure but different stability in the yeast linker histone, Hho1p. *J. Mol. Biol.*, **338**, 139–48.
19. Cerf, C., Lippens, G., Ramakrishnan, V., Muyldermans, S., Segers, A., Wyns, L., Wodak, S. and Hallenga, K. (1994) Homo- and heteronuclear two-dimensional NMR studies of the globular domain of histone H1: full assignment, tertiary structure, and comparison with the globular domain of histone H5. *Biochemistry*, **33**, 11079–11086.
20. Allan, J., Hartman, P. and Crane-Robinson, C. (1980) The structure of histone H1 and its location in chromatin. *Nature*, **288**, 675–679.
21. Bharath, M., Chandra, N. and Rao, M. (2003) Molecular modeling of the chromatosome particle. *Nucleic Acids Res.*, **31**, 4264–4274.
22. Fan, L. and Roberts, V. (2006) Complex of linker histone H5 with the nucleosome and its implications for chromatin packing. *Proc. Natl. Acad. Sci. U.S.A.*, **103**, 8384–8389.
23. Zhou, B.-R., Feng, H., Kato, H., Dai, L., Yang, Y., Zhou, Y. and Bai, Y. (2013) Structural insights into the histone H1-nucleosome complex. *Proc. Natl. Acad. Sci. U.S.A.*, **110**, 19390–19395.
24. Allan, J., Mitchell, T., Harborne, N., Bohm, L. and Crane-Robinson, C. (1986) Roles of H1 domains in determining higher order chromatin structure and H1 location. *J. Mol. Biol.*, **187**, 591–601.
25. Hansen, J., Lu, X., Ross, E. and Woody, R. (2006) Intrinsic protein disorder, amino acid composition, and histone terminal domains. *J. Biol. Chem.*, **281**, 1853–1856.
26. Ponte, L., Vila, R. and Suau, P. (2003) Sequence complexity of histone H1 subtypes. *Mol. Biol. Evol.*, **20**, 371–380.
27. Hendzel, M., Lever, M., Crawford, E. and Th'ng, J. (2004) The C-terminal domain is the primary determinant of histone H1 binding to chromatin in vivo. *J. Biol. Chem.*, **279**, 20028–20034.
28. Fang, H., Clark, D. and Hayes, J. (2012) DNA and nucleosomes direct distinct folding of a linker histone H1 C-terminal domain. *Nucleic Acids Res.*, **40**, 1475–1484.
29. Bharath, M., Chandra, N. and Rao, M. (2002) Prediction of an HMG-box fold in the C-terminal domain of histone H1: insights into its role in DNA condensation. *Proteins*, **49**, 71–81.
30. Schlick, T., Collepardo-Guevara, R., Halvorsen, L., Jung, S. and Xiao, X. (2011) Biomolecular modeling and simulation: a field coming of age. *Q. Rev. Biophys.*, **44**, 191–228.
31. Schlick, T. (2013) The 2013 Nobel Prize in chemistry celebrates computations in chemistry and biology. *SIAM News*, **46**, 10.
32. Pachov, G., Gabbouline, R. and Wade, R. (2011) On the structure and dynamics of the complex of the nucleosome and the linker histone. *Nucleic Acids Res.*, **39**, 5255–5263.
33. Arya, G. and Schlick, T. (2009) A tale of tails: how histone tails mediate chromatin compaction in different salt and linker histone environments. *J. Phys. Chem. A*, **113**, 4045–4059.
34. Collepardo-Guevara, R. and Schlick, T. (2014) Chromatin fiber polymorphism triggered by variations of DNA linker lengths. *Proceedings of the National Academy of Sciences of the United States of America*.
35. Collepardo-Guevara, R. and Schlick, T. (2012) Crucial role of dynamic linker histone binding and divalent ions for DNA accessibility and gene regulation revealed by mesoscale modeling of oligonucleosomes. *Nucleic Acids Res.*, **40**, 8803–8817.
36. Collepardo-Guevara, R. and Schlick, T. (2011) The effect of linker histone's nucleosome binding affinity on chromatin unfolding mechanisms. *Biophysical Journal* **101**, 1670–1680.
37. Schlick, T. and Perišić, O. (2009) Mesoscale simulations of two nucleosome-repeat length oligonucleosomes. *Phys. Chem. Chem. Phys.*, **11**, 10729–10737.
38. Song, F., Chen, P., Sun, D., Wang, M., Dong, L., Liang, D., Xu, R.-M., Zhu, P. and Li, G. (2014) Cryo-EM study of the chromatin fiber reveals a double helix twisted by tetranucleosomal units. *Science*, **344**, 376–380.
39. Zhang, Q., Beard, D. and Schlick, T. (2003) Constructing irregular surfaces to enclose macromolecular complexes for mesoscale modeling using the discrete surface charge optimization (DiSCO) algorithm. *J. Comput. Chem.*, **24**, 2063–2074.
40. Stigter, D. (1977) Interactions of highly charged colloidal cylinders with applications to double-stranded. *Biopolymers*, **16**, 1435–1448.
41. Schlick, T., Li, B. and Olson, W.K. (1994) The influence of salt on the structure and energetics of supercoiled DNA. *Biophys. J.*, **67**, 2146–2166.
42. Xiao, B., Freedman, B.S., Miller, K.E., Heald, R. and Marko, J.F. (2012) Histone H1 compacts DNA under force and during chromatin assembly. *Mol. Biol. Cell*, **67**, 2146–2166.
43. Yin, Y., Arkhipov, A. and Schulten, K. (2009) Simulations of membrane tubulation by lattices of amphiphysin N-BAR domains. *Structure*, **17**, 882–892.
44. Humphrey, W., Dalke, A. and Schulten, K. (1996) VMD—visual molecular dynamics. *J. Mol. Graph.*, **14**, 33–38.
45. Woodcock, C.L., Skoultchi, A.I. and Fan, Y. (2006) Role of linker histone in chromatin structure and function: H1 stoichiometry and nucleosome repeat length. *Chromosome Res.*, **14**, 17–25.
46. Scheffer, M., Eltsov, M., Bednar, J. and Frangakis, A. (2012) Nucleosomes stacked with aligned dyad axes are found in native compact chromatin in vitro. *J. Struct. Biol.*, **178**, 207–214.
47. Artimo, P., Jonnalagedda, M., Arnold, K., Baratin, D. and Csardi, E.A. (2012) ExPASy: SIB bioinformatics resource portal. *Nucleic Acids Res.*, **40**, W597–W603.
48. Nikitina, T., Wang, D., Gomberg, M., Grigoryev, S. and Zhurkin, V. (2013) Combined micrococcal nuclease and exonuclease III digestion reveals precise positions of the nucleosome core/linker junctions: implications for high-resolution nucleosome mapping. *J. Mol. Biol.*, **425**, 1946–1960.
49. Carruthers, L., Bednar, J., Woodcock, C.L. and Hansen, J.C. (1998) Linker histones stabilize the intrinsic salt-dependent folding of nucleosomal arrays: mechanistic ramifications for higher-order chromatin folding. *Biochemistry*, **37**, 14776–14787.
50. Butler, P. and Thomas, J. (1980) Changes in chromatin folding in solution. *J. Mol. Biol.*, **140**, 505–529.
51. Scheffer, M., Eltsov, M. and Frangakis, A. (2011) Evidence for short-range helical order in the 30-nm chromatin fibers of erythrocyte nuclei. *Proc. Natl. Acad. Sci. U.S.A.*, **108**, 16992–16997.
52. Bergman, M., Wawra, E. and Winge, M. (1988) Chicken histone H5 inhibits transcription and replication when introduced into proliferating cells by microinjection. *J. Cell Sci.*, **91**, 201–209.
53. Eltsov, M., Maclellan, K., Maeshima, K., Frangakis, A. and Dubochet, J. (2008) Analysis of cryo-electron microscopy images does not support the existence of 30-nm chromatin fibers in mitotic chromosomes in situ. *Proc. Natl. Acad. Sci. U.S.A.*, **105**, 19732–19737.
54. Brown, D., Izard, T. and Misteli, T. (2006) Mapping the interaction surface of linker histone H1(0) with the nucleosome of native chromatin in vivo. *Nat. Struct. Mol. Biol.*, **13**, 250–255.
55. Wisniewski, J., Zougman, A., Krüger, S. and Mann, M. (2007) Mass spectrometric mapping of linker histone H1 variants reveals multiple acetylations, methylations, and phosphorylation as well as differences between cell culture and tissue. *Mol. Cell. Proteomics*, **6**, 72–87.
56. Dou, Y. and Gorovsky, M. (2002) Regulation of transcription by H1 phosphorylation in *Tetrahymena* is position independent and requires clustered sites. *Proc. Natl. Acad. Sci. U.S.A.*, **99**, 6142–6146.
57. Maria, A., Christophorou, Castelo-Branco, Gonçalves, Richard, P. Halley-Stott, Slade Oliveira, Clara, Loos, Remco, Radzishuskaya, Aliaksandra, Kerri, A. Mowen, Bertone, Paul, C R Silva, José, Zernicka-Goetz, Magdalena, L Nielsen, Michael, B Gurdon, John and Kouzarides, Tony (2014) Citrullination regulates pluripotency and histone H1 binding to chromatin. *Nature* **507**, 104–108 [PubMed].
58. Roth, S.Y. and Allis, C.D. (1992) Chromatin condensation: does histone H1 dephosphorylation play a role? *Trends Biochem. Sci.*, **17**, 93–98.